Letter

Large momentum transfer Raman atom interferometer without k-reversal

Guanchen Peng, Bryony Lanigan, R. Shah, J. Lim, A. Kaushik, J. P. Cotter, E. A. Hinds, and B. E. Sauer*

Centre for Cold Matter, Blackett Laboratory, Imperial College London, Prince Consort Road, London SW7 2AZ, United Kingdom

(Received 13 February 2025; accepted 21 July 2025; published 25 August 2025)

We present a Raman atom interferometer using large momentum transfer without reversing the direction of the effective wave vector (k-reversal). More specifically, we use a microwave $\pi/2$ pulse to manipulate the spin state of ^{87}Rb atoms before applying a Raman light π pulse to achieve $4\hbar k$ momentum transfer per Raman light pulse. A microwave π pulse in the middle of the interferometer sequence reverses the spin states, which allows closing of the interferometer arms by the same Raman light π pulses without propagation reversal. We present a proof-of-principle demonstration of a $4\hbar k$ large-momentum-transfer (LMT) atom interferometer and discuss its scalability. Our results extend the scope of using LMT atom optics.

DOI: 10.1103/ghlb-v3jc

Atom interferometers have emerged as pivotal tools in modern physics, enabling high-precision measurements of fundamental constants [1–5], rigorous tests of physical laws [6–9], and ambitious efforts to detect dark energy [10,11], dark matter, or gravitational waves [12–15]. In these measurements, light is used to split an atomic wave packet, which then propagates along two distinct interferometer arms, before being recombined to obtain interference fringes that are sensitive to the acceleration of the atom. The exchange of momentum with the light can entangle the two momentum states of the atom with two different internal states, simplifying detection of the fringes by eliminating the need to resolve the two output ports spatially. Raman transitions between hyperfine ground states have proved to be an effective way of doing this in technological applications, including inertial sensing [16–20] and gravity mapping [21–24].

The acceleration sensitivity of an atom interferometer increases with the space-time area enclosed by the arms. One method to increase sensitivity, therefore, is to increase the propagation time. In free fall (as opposed to trapped geometries, e.g., Ref. [25]), propagation times have been extended by the use of atomic fountains [16,26,27], drop towers [28,29], and other micro-g environments [30–33]. These approaches allow longer free-fall times, but at the expense of large infrastructure, increasing the scale and complexity of experiments. An alternative is to increase the momentum imparted to the atom by the beam splitter. Large-momentum-transfer (LMT) methods have achieved differential momenta as high as $16\hbar k$ using spin-dependent Raman kicks [34], $100\hbar k$ using sequential Bragg atom optics [35], and $400\hbar k$ using a combination of Bloch oscillations and Bragg transitions in twin optical lattices [36].

Unlike LMT methods using Bragg diffraction or Bloch oscillations, LMT Raman atom interferometers [34,37] need to reverse the direction, κ, of the effective wave vector between successive light pulses. The effective wave vector of both directions is present in Ref. [34], but the Doppler shift resolves the degeneracy of the Raman resonances for $\kappa = \pm 1$. It is necessary therefore to switch rapidly between different frequencies during one interferometer sequence, while preserving phase coherence [38]. In vertical accelerometers, the velocity of atoms falling under gravity naturally lifts the degeneracy. In horizontal accelerometers, the atoms can be launched with enough velocity to lift the degeneracy [39], at the cost of some technical complexity. This complexity can be avoided by removing one of the retroreflected Raman beams [40,41], but then it is not possible to reverse κ.

We present a different method for achieving LMT in a Raman atom interferometer without the need for k-reversal. Our method closely follows the work in Ref. [34], but we eliminate the need for reversing κ by employing a sequence of alternating microwave and optical transitions. This approach also removes the need to switch the frequency of the light pulses rapidly within a single interferometer sequence. It shares the benefit of being insensitive to ac Stark shifts as only π pulses are used [42]. We demonstrate an implementation of this method and propose a pathway toward achieving larger momentum transfers, enabling even greater sensitivities.

Our realization of the interferometer scheme uses ^{87}Rb atoms. As shown in Fig. 1(a), we use microwave pulses to directly couple the hyperfine levels of the $(5s)^2S_{1/2}$ state, and laser pulses detuned from the $(5p)^2P_{3/2}$ state to drive Raman transitions between these levels. Our $4\hbar k$ LMT atom interferometer is realized by three microwave pulses and four Raman pulses, as is illustrated in Fig. 1(b). The interferometer sequence starts with a spin-dependent-kick beam splitter [34]. This uses a microwave $\pi/2$ pulse followed by a Raman π pulse to create a momentum separation between two

*Contact author: ben.sauer@imperial.ac.uk

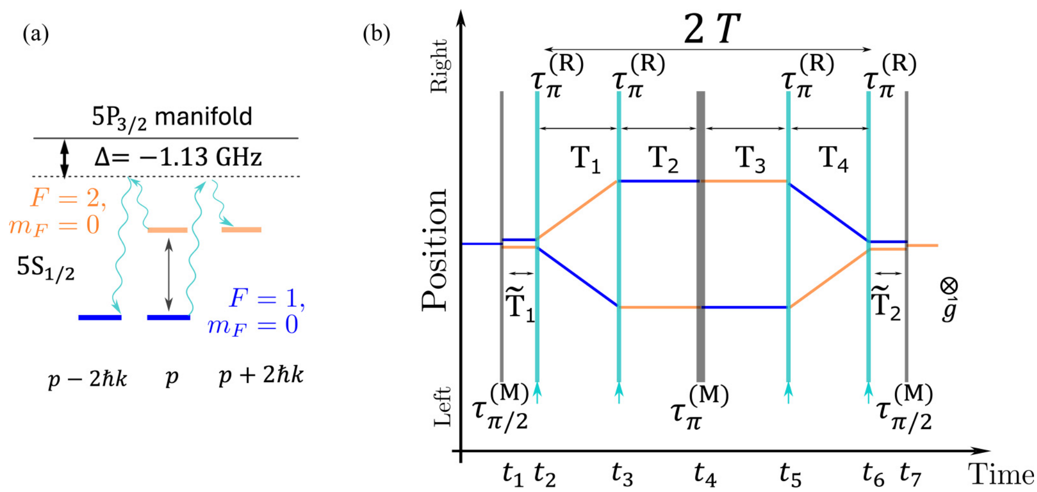

FIG. 1. A $4\hbar k$ large momentum transfer without k-reversal. (a) Energy-momentum states involved in the interferometer. We drive Raman transitions (cyan arrows) and microwave transitions (gray arrow) between $|F = 1, m_F = 0\rangle$ and $|F = 2, m_F = 0\rangle$ to induce spin-dependent kicks. (b) A $4\hbar k$ large momentum transfer interferometer. The microwave interaction (gray lines) couples spin states of the same momentum state. The Raman interaction (cyan lines) couples different momentum states by spin-dependent momentum transfer.

interferometer arms of $4\hbar k$, where $k = 2\pi/\lambda$ and $\lambda \approx 780$ nm. More specifically, the microwave $\pi/2$ pulse puts each atom into an equal superposition of two spin states, $|F, m_F\rangle = |1, 0\rangle$ and $|2, 0\rangle$, without changing its momentum state. After a period $\widetilde{T}_1$ of free evolution, a Raman π pulse imparts momenta of $+2\hbar k$ to $|1, 0\rangle$ and $-2\hbar k$ to $|2, 0\rangle$, as well as reversing the spin states. A second Raman π pulse is applied after a further time T_1. This keeps the spatial separation between the two interferometer arms at a fixed distance, $d = 4\hbar k T_1/M$, where M is the atomic mass. The atoms then evolve freely for a time T_2 before the spin states of the two arms are swapped by a microwave π pulse. Subsequently, there is another free evolution time T_3, following which the two interferometer arms are closed, *without k-reversal*, by applying two more Raman π pulses separated by $T_4 = T_1$. Finally, after freely evolving for $\widetilde{T}_2$, the two arms are made to interfere by applying the last microwave $\pi/2$ pulse.

After the interferometer sequence described above, the population in $|2, 0\rangle$, $P_{F=2}$, is

$$P_{F=2} = B - A\cos(\Delta\phi^{\mathrm{M}} + \Delta\phi^{\mathrm{R}}), \tag{1}$$

where B is the middle point of the interference fringe, A is the amplitude of the fringe, and $\Delta\phi^{\mathrm{M}}$ and $\Delta\phi^{\mathrm{R}}$ are the phase differences along the two paths due to interactions with the microwave and Raman fields, respectively.

The full derivation of $\Delta\phi^{\mathrm{M}}$ and $\Delta\phi^{\mathrm{R}}$ can be found in the Supplemental Material [43]. Here we choose $T_1 = T_4$ in order to close the interferometer. The microwave phase difference is then

$$\Delta\phi^{\mathrm{M}} = (\omega^{\mathrm{M}} - \omega_0)(\widetilde{T}_1 + T_2 - T_3 - \widetilde{T}_2), \tag{2}$$

where ω^{M} is the microwave frequency and ω_0 is the hyperfine splitting of the $(5s)^2S_{1/2}$ state. We choose a symmetric timing of $\widetilde{T}_1 = \widetilde{T}_2$ and $T_2 = T_3$ to ensure that $\Delta\phi^{\mathrm{M}}$ is strongly suppressed. With this timing, the Raman phase, calculated in the short-pulse limit [26,44], is

$$\Delta\phi^{\mathrm{R}} = a\,\frac{T_1}{T}\left(2 - \frac{T_1}{T}\right)4kT^2 = ankT^2, \tag{3}$$

where a is the constant acceleration of the atom relative to the retroreflection mirror, projected onto the axis of Raman beam propagation. The $4k$ factor originates from the $4\hbar k$ differential momentum transfer per Raman pulse, and $2T = T_1 + T_2 + T_3 + T_4$ is the interval between the first and the last Raman pulse. The dimensionless factor n is a simple way of characterizing the sensitivity to acceleration for a given value of T_1/T. We note that, in the limit of $T_1/T \to 0$, Eq. (3) gives $n_{\mathrm{LMT}} \to 0$, and the interferometer has no acceleration sensitivity. In this limit, the two paths enclose no area, and the interferometer becomes a microwave spin-echo sequence. In the limit of $T_1/T \to 1$, the interferometer reaches its maximum acceleration sensitivity of $n_{\mathrm{LMT}} \to 4$ as the space-time area enclosed is the maximum available with a $4\hbar k$ momentum transfer. In this Letter, we study the phase $\Delta\phi^{\mathrm{R}}$, defined in Eq. (3), and compare it with that of a standard three-pulse Mach-Zehnder (MZ) atom interferometer.

The apparatus is very similar to that described in Ref. [40]. Here we give a brief description of the experimental sequence. Approximately 10^8 atoms of ^{87}Rb are cooled to $\sim 10\,\mu$K and optically pumped into the $(5s)^2S_{1/2}$ $F = 1$ ground state, distributed across the three m_F sublevels. A state preparation sequence, outlined in the Supplemental Material [43] and in Ref. [41], drives approximately 5×10^6 of the atoms into the magnetically insensitive $|1, 0\rangle$ state and removes the rest. During the interferometer sequence, we apply a bias magnetic field to lift the degeneracy of the m_F states. Laser light is provided by the μQuans system described in Ref. [40]. The Raman frequencies, ω_1 and ω_2, differ by $2\pi \times 6.834$ GHz in order to drive the hyperfine transition $|F, m_F\rangle = |1, 0\rangle \to |2, 0\rangle$.

Figure 2 shows the preparation of the light for the interferometer. The light at the two Raman frequencies $\omega_1(\omega_2)$ leaves

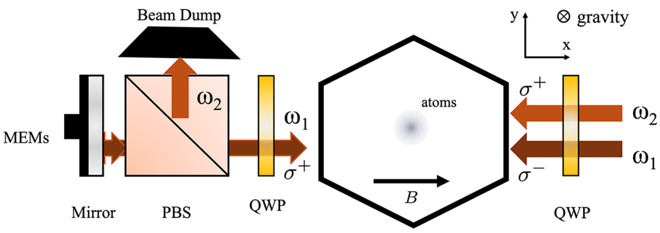

FIG. 2. Schematic of the Raman beam setup, showing the polarization scheme that rejects the counterpropagating ω_2 light, to only drive the σ^+–σ^+ Raman transition. See main text for details.

the output fiber with orthogonal linear polarizations, before passing through a quarter-wave plate (QWP) to become right-handed (left-handed) circular polarizations that drive $\sigma^-(\sigma^+)$ transitions. After passing through another QWP, ω_2 is directed to a beam dump by a polarizing beam splitter (PBS) while ω_1 passes through, reflects from the mirror, and passes back through the PBS and the QWP resulting in a right-handed circular polarization, which completes the σ^+–σ^+ Raman transition. As ω_2 is rejected, the σ^-–σ^- Raman transition is not driven [45]. A horn delivers microwave radiation to the atoms through a vacuum window. The microwave source is derived from the μQuans Raman laser system so that the radiation is phase-coherent with the beat note between the two Raman beams, as is necessary to form the interferometer. A microelectromechanical (MEMS) accelerometer is attached to the rear of the mirror to monitor its vibrations.

The interferometer scheme is shown in Fig. 1(b), with $\widetilde{T}_1 = \widetilde{T}_2 = 1$ ms and $T_1 \cdots T_4$, all set to 4 ms. The fraction of atoms in the $F = 2$ state, $P_{F=2}$, is determined by state-sensitive fluorescence detection.

The orange points in Fig. 3 show $P_{F=2}$ measured as a function of the mirror acceleration [46]. Each point in the plot is an average of either 40 or 4 measurements, and the error bar in $P_{F=2}$ represents the standard deviation of the mean of those measurements. No error bars are shown for the acceleration

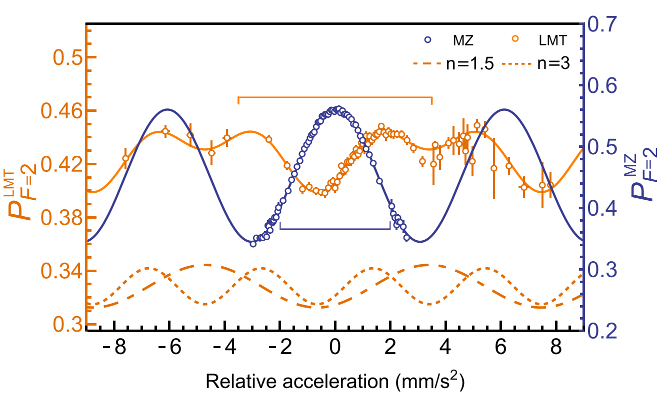

FIG. 3. Atom interferometer fringes with $T = 8$ ms, shifted to be centered near zero acceleration. Orange data points: LMT interferometer. Blue points: three-pulse Mach-Zehnder interferometer. In the range indicated by the orange (blue) bracket, each orange (blue) point is the average of 40 measurements. Outside those ranges, each point is the average of four measurements. Solid curves: fits to Eqs. (4) and (5). Dashed and dotted curves: separate contributions in the fit from main and parasitic interferometers, respectively (arbitrarily lowered for clarity).

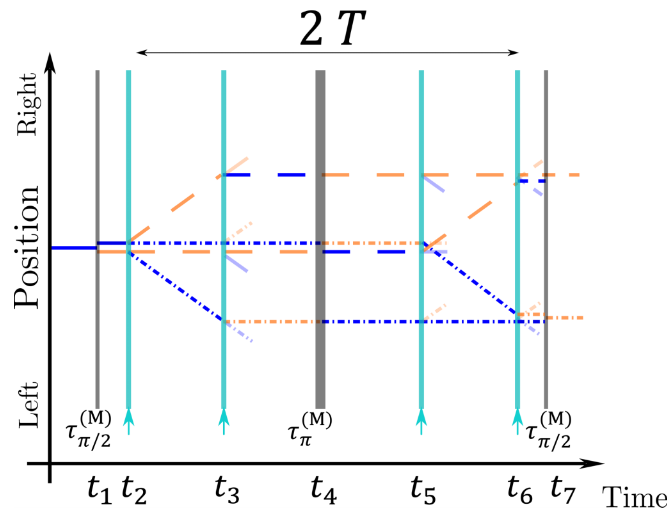

FIG. 4. Parasitic interferometers in the scheme of Fig. 1(b). These form because the Raman pulse is not a perfect π pulse. The dotted/dashed lines show the two closed paths with zero-momentum output states. Orange (blue) lines indicate $F = 2$ ($F = 1$) states. Faint lines indicate the starts of other paths.

as these are all less than 0.5 mm/s^2. For each measurement, the mirror acceleration $\langle a(t)\rangle_{\rm LMT}$ is averaged over the time between the first and last Raman pulses, with a trapezoidal weighting, as described in the Supplemental Material [43] (see also references [44,47,48] therein). The range of accelerations plotted in Fig. 3 is passively sampled by the free movements of the laser table and the mirror. In order to achieve a scan this wide, the table was not floated.

For comparison, the blue points in Fig. 3 are taken using a three-pulse MZ sequence with the same $T = 8$ ms and the standard triangular weighting function to obtain the time-averaged mirror acceleration $\langle a(t)\rangle_{\rm MZ}$ [48]. These data were taken with the table floating. We fit the MZ interference fringe to the function

$$P^{\rm MZ}_{F=2} = B - A\cos\left(n_{\rm MZ}\,\langle a(t)\rangle_{\rm MZ}\,k\,T^2 + \phi_0\right), \tag{4}$$

where ϕ_0 is an offset phase, with the result plotted in Fig. 3. This gives $n_{\rm MZ} = 2.00 \pm 0.01$, which is in excellent agreement with the expected value of 2 due to the $2\hbar k$ momentum transfer per Raman pulse.

In contrast, it is clear from the orange data in Fig. 3 that the LMT interferometer does not exhibit the single sinusoidal behavior proposed in Eq. (1). This more complicated fringe pattern is due to the two additional parasitic interferometers shown in Fig. 4, which arise because the Raman pulses are not exactly π pulses. This is unavoidable as the intensity of the Raman beams varies across the cloud of atoms. These parasitic interferometers require the same trapezoidal acceleration weighting function as the LMT interferometer, but have only half the acceleration sensitivity because they enclose half the area. More parasitic interferometers are created in a similar way by the other imperfect Raman pulses, but they involve higher momenta that are outside the linewidth of the Raman transition, and are too weak to see. We note that the two arms of the main $4\hbar k$ LMT interferometer have opposite two-photon recoil shifts of $\pm 2\pi \times 15$ kHz. Our Raman coupling

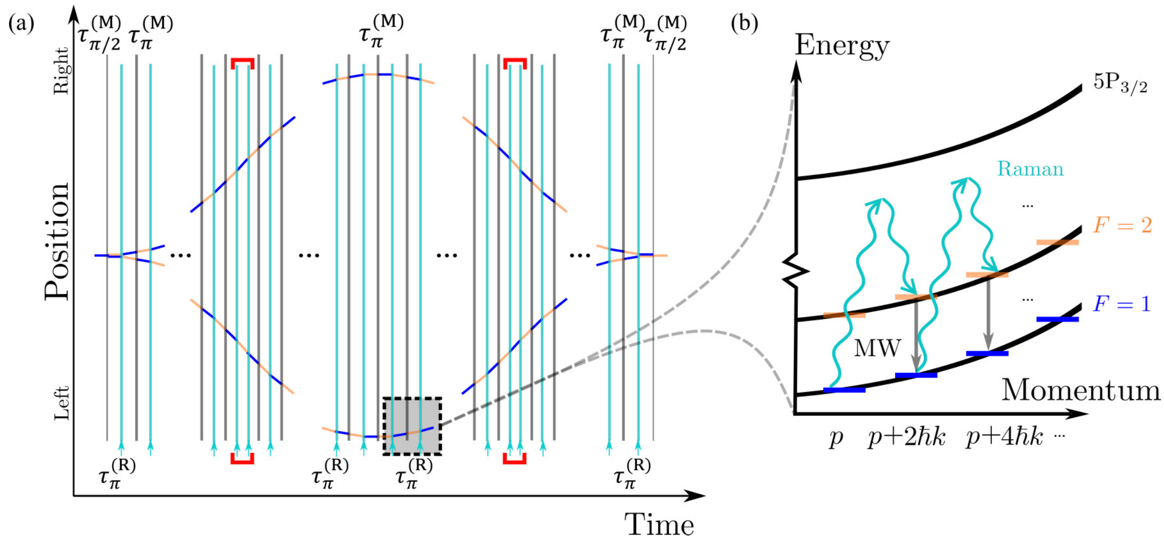

FIG. 5. Proposed extension from Fig. 1(b) to a $4N\hbar k$ interferometer without k-reversal. (a) Schematic of the pulse timing. The two interferometer arms are opened and closed by microwave $\pi/2$ pulses (thin gray lines). All the Raman pulses (cyan solid lines) are π pulses to induce spin-dependent momentum transfer, before microwave π pulses (thick gray lines) swap their internal states without affecting the momentum. Note the paired Raman pulses at the center of the second and fourth sections (highlighted in red). These reverse the order of the alternating Raman and microwave sequence, as is necessary to reverse the acceleration between the two arms. The central microwave π pulse not only equalizes the time spent by each spin state on two arms, but also closes the interferometer without k-reversal. (b) Energy-momentum states of one of the interferometer arms during part of the pulse sequence. The two-step transfer is analogous to a Bragg transition.

of $2\pi \times 50\,\text{kHz}$ is just sufficient to drive transitions in both of these arms simultaneously.

In order to describe this more complicated fringe, we fitted the data to the function

$$P^{\text{LMT}}_{F=2} = B - A_1 \cos\left(n^{(1)}_{\text{LMT}} \langle a(t)\rangle_{\text{LMT}} k T^2 + \phi_1\right) - A_2 \cos\left(n^{(2)}_{\text{LMT}} \langle a(t)\rangle_{\text{LMT}} k T^2 + \phi_2\right), \quad (5)$$

where A_i, B, $n^{(i)}_{\text{LMT}}$, and ϕ_i are fitting parameters ($i = 1$ for the desired interferometer and $i = 2$ for the parasitic ones). The fit, plotted in Fig. 3, gives $n^{(1)}_{\text{LMT}} = 3.00 \pm 0.05$ in good agreement with the value expected for the main interferometer by putting $T_1/T = 1/2$ into Eq. (3). This result confirms that the LMT interferometer does indeed have a finer fringe spacing than that of the three-pulse Mach-Zehnder interferometer by a factor of 1.5 for the same time T. It also verifies that the trapezoidal acceleration weighting function is valid. We expect $n^{(2)}_{\text{LMT}} = \frac{1}{2} n^{(1)}_{\text{LMT}}$ because the parasitic interferometers enclose half the area, and that is confirmed by the same fit, which yields $n^{(2)}_{\text{LMT}} = 1.50 \pm 0.04$.

The dashed and dash-dotted lines in Fig. 3 show the separate contributions to the fit from the main and parasitic interferometers. We see that the minima of the parasitic fringes coincide with every second minimum of the main interferometer. This is to be expected if ϕ_1 and ϕ_2 simply represent our arbitrary choice of zero relative acceleration. In that case, we would expect $\phi_1 = 2\phi_2$, and indeed the fit gives $1.01 \pm 0.06\,\text{rad}$ and $0.51 \pm 0.06\,\text{rad}$. This proportionality serves as a useful test to show that our interferometer does not suffer from phase errors that depend differently on the enclosed area, e.g., light shifts or Zeeman shifts.

It is instructive to compare the peak-to-peak amplitudes of the Mach-Zehnder and LMT fringes in Fig. 3. The former uses three Raman pulses: $\pi/2$, π, $\pi/2$. Averaged over the cloud of atoms, the Raman π pulse makes a transition probability of only 0.55. As a rough estimate, we can therefore expect a peak-to-peak amplitude of order $(0.55)^3$, which is close to the 0.2 that we observe. In contrast, the LMT interferometer requires seven pulses: three microwave pulses, for which the population transfer efficiency is ~ 0.8, and four Raman π pulses. The rough estimate of $(0.8)^3 \times (0.55)^4$ is similar to the measured peak-to-peak amplitude of ~ 0.03.

Figure 5 shows how to extend our method to larger recoils of $N \times 4\hbar k$ without k-reversal. Figure 5(a) shows the overall pulse scheme, while Fig. 5(b) shows how the paired Raman and microwave pulses increase the momentum. The analogy with Bragg transitions is discussed in the Supplemental Material [43]. The numbers of microwave and Raman pulses scale as $(4N - 1)$ and $4N$, respectively, so both will need to be more efficient. At present, the microwave field is inhomogeneous because of standing waves formed by reflections within the vacuum chamber, but with a redesign, one could approach the ideal of a plane wave perpendicular to the Raman axis. The Raman π pulse efficiency is low because of the intensity variations across the Gaussian laser beam. This difficulty can be removed by using the adiabatic-passage technique described in Ref. [34], which overcomes both the intensity variations and the opposite recoil shifts of the two interferometer arms. With a pulse efficiency of 96%, similar to that shown in Ref. [34], one can expect our scheme to achieve a recoil of $16\hbar k$ and a fringe peak-to-peak amplitude of ~ 0.3, which is similar to the amplitude in Ref. [34].

The resulting improvement in sensitivity to accelerations would be valuable in several applications. Examples include compact low-drift accelerometers for navigation [16–20] and fundamental physics experiments, such as gravitational wave detection using a pair of horizontal accelerometers [12,13]. In these applications, our method allows enhancing acceleration sensitivity without rapidly switching κ in one measurement; however, it will be useful to reverse κ from one measurement to the next. The two phases $(+nkaT^2 + \varphi)$ and $(-nkaT^2 + \varphi)$ would reveal the presence of any unwanted phase φ that does not depend on the sign of κ.

In summary, we have demonstrated an approach that removes the need to reverse κ when applying spin-dependent momentum kicks in atom interferometry [34]. Our approach still retains the benefits of the original proposal, namely (1) insensitivity to the ac Stark shifts by limiting the light to π pulses and (2) encoding of the momentum states in the internal states to enable readout.

We acknowledge engineering support by J. Dyne, software support by Teodor B. Krastev, and inspiring discussions with Malo Cadoret (Conservatoire National des Arts et Métiers, Paris, France). We thank the UK Science and Technology Facilities Council (STFC) for funding through Grants No. ST/W006316/1 and No. ST/V00428X/1.

Data Availability. The data that support the findings of this article are openly available [46].

[1] J. B. Fixler, G. T. Foster, J. M. McGuirk, and M. A. Kasevich, Atom interferometer measurement of the Newtonian constant of gravity, Science **315**, 74 (2007).

[2] G. Rosi, F. Sorrentino, L. Cacciapuoti, M. Prevedelli, and G. M. Tino, Precision measurement of the Newtonian gravitational constant using cold atoms, Nature (London) **510**, 518 (2014).

[3] R. Bouchendira, P. Cladé, S. Guellati-Khélifa, F. Nez, and F. Biraben, New determination of the fine structure constant and test of the quantum electrodynamics, Phys. Rev. Lett. **106**, 080801 (2011).

[4] R. H. Parker, C. Yu, W. Zhong, B. Estey, and H. Müller, Measurement of the fine-structure constant as a test of the standard model, Science **360**, 191 (2018).

[5] L. Morel, Z. Yao, P. Cladé, and S. Guellati-Khélifa, Determination of the fine-structure constant with an accuracy of 81 parts per trillion, Nature (London) **588**, 61 (2020).

[6] D. Schlippert, J. Hartwig, H. Albers, L. L. Richardson, C. Schubert, A. Roura, W. P. Schleich, W. Ertmer, and E. M. Rasel, Quantum test of the universality of free fall, Phys. Rev. Lett. **112**, 203002 (2014).

[7] L. Zhou, S. Long, B. Tang, X. Chen, F. Gao, W. Peng, W. Duan, J. Zhong, Z. Xiong, J. Wang, Y. Zhang, and M. Zhan, Test of equivalence principle at 10^{-8} level by a dual-species double-diffraction Raman atom interferometer, Phys. Rev. Lett. **115**, 013004 (2015).

[8] T. Zhang, L.-L. Chen, Y.-B. Shu, W.-J. Xu, Y. Cheng, Q. Luo, Z.-K. Hu, and M.-K. Zhou, Ultrahigh-sensitivity Bragg atom gravimeter and its application in testing Lorentz violation, Phys. Rev. Appl. **20**, 014067 (2023).

[9] C. Overstreet, P. Asenbaum, J. Curti, M. Kim, and M. A. Kasevich, Observation of a gravitational Aharonov-Bohm effect, Science **375**, 226 (2022).

[10] C. Burrage, E. J. Copeland, and E. Hinds, Probing dark energy with atom interferometry, J. Cosmol. Astropart. Phys. 03 (2015) 042.

[11] C. D. Panda, M. J. Tao, M. Ceja, J. Khoury, G. M. Tino, and H. Müller, Measuring gravitational attraction with a lattice atom interferometer, Nature (London) **631**, 515 (2024).

[12] B. Canuel, A. Bertoldi, L. Amand, E. Pozzo di Borgo, T. Chantrait, C. Danquigny, M. Dovale Álvarez, B. Fang, A. Freise, R. Geiger, J. Gillot *et al.*, Exploring gravity with the MIGA large scale atom interferometer, Sci. Rep. **8**, 14064 (2018).

[13] M.-S. Zhan, J. Wang, W.-T. Ni, D.-F. Gao, G. Wang, L.-X. He, R.-B. Li, L. Zhou, X. Chen, J.-Q. Zhong, B. Tang *et al.*, ZAIGA: Zhaoshan long-baseline atom interferometer gravitation antenna, Int. J. Mod. Phys. D **29**, 1940005 (2020).

[14] L. Badurina *et al.*, AION: An atom interferometer observatory and network, J. Cosmol. Astropart. Phys. 05 (2020) 011.

[15] M. Abe, P. Adamson, M. Borcean, D. Bortoletto, K. Bridges, S. P. Carman, S. Chattopadhyay, J. Coleman, N. M. Curfman, K. DeRose *et al.*, Matter-wave atomic gradiometer interferometric sensor (MAGIS-100), Quantum Sci. Technol. **6**, 044003 (2021).

[16] S. M. Dickerson, J. M. Hogan, A. Sugarbaker, D. M. S. Johnson, and M. A. Kasevich, Multiaxis inertial sensing with long-time point source atom interferometry, Phys. Rev. Lett. **111**, 083001 (2013).

[17] Q. d'Armagnac de Castanet, C. Des Cognets, R. Arguel, S. Templier, V. Jarlaud, V. Ménoret, B. Desruelle, P. Bouyer, and B. Battelier, Atom interferometry at arbitrary orientations and rotation rates, Nat. Commun. **15**, 6406 (2024).

[18] R. Geiger, V. Ménoret, G. Stern, N. Zahzam, P. Cheinet, B. Battelier, A. Villing, F. Moron, M. Lours, Y. Bidel *et al.*, Detecting inertial effects with airborne matter-wave interferometry, Nat. Commun. **2**, 474 (2011).

[19] P. Cheiney, L. Fouché, S. Templier, F. Napolitano, B. Battelier, P. Bouyer, and B. Barrett, Navigation-compatible hybrid quantum accelerometer using a Kalman filter, Phys. Rev. Appl. **10**, 034030 (2018).

[20] S. Templier, P. Cheiney, Q. d'Armagnac de Castanet, B. Gouraud, H. Porte, F. Napolitano, P. Bouyer, B. Battelier, and B. Barrett, Tracking the vector acceleration with a hybrid quantum accelerometer triad, Sci. Adv. **8**, eadd3854 (2022).

[21] B. Stray *et al.*, Quantum sensing for gravity cartography, Nature (London) **602**, 590 (2022).

[22] C.-Y. Li, J.-B. Long, M.-Q. Huang, B. Chen, Y.-M. Yang, X. Jiang, C.-F. Xiang, Z.-L. Ma, D.-Q. He, L.-K. Chen, and S. Chen, Continuous gravity measurement with a portable atom gravimeter, Phys. Rev. A **108**, 032811 (2023).

[23] V. Ménoret, P. Vermeulen, N. Le Moigne, S. Bonvalot, P. Bouyer, A. Landragin, and B. Desruelle, Gravity measurements

below $10^{-9}g$ with a transportable absolute quantum gravimeter, Sci. Rep. **8**, 12300 (2018).
[24] X. Wu, Z. Pagel, B. S. Malek, T. H. Nguyen, F. Zi, D. S. Scheirer, and H. Müller, Gravity surveys using a mobile atom interferometer, Sci. Adv. **5**, eaax0800 (2019).
[25] C. D. Panda, M. Tao, J. Egelhoff, M. Ceja, V. Xu, and H. Müller, Coherence limits in lattice atom interferometry at the one-minute scale, Nat. Phys. **20**, 1234 (2024).
[26] M. Kasevich and S. Chu, Measurement of the gravitational acceleration of an atom with a light-pulse atom interferometer, Appl. Phys. B **54**, 321 (1992).
[27] A. Clairon, C. Salomon, S. Guellati, and W. D. Phillips, Ramsey resonance in a Zacharias fountain, Europhys. Lett. **16**, 165 (1991).
[28] S. Kulas, C. Vogt, A. Resch, J. Hartwig, S. Ganske, J. Matthias, D. Schlippert, T. Wendrich, W. Ertmer, E. Maria Rasel *et al.*, Miniaturized lab system for future cold atom experiments in microgravity, Microgravity Sci. Technol. **29**, 37 (2017).
[29] H. Müntinga *et al.*, Interferometry with Bose-Einstein condensates in microgravity, Phys. Rev. Lett. **110**, 093602 (2013).
[30] J. R. Williams *et al.*, Pathfinder experiments with atom interferometry in the cold atom lab onboard the International Space Station, Nat. Commun. **15**, 6414 (2024).
[31] M. D. Lachmann, H. Ahlers, D. Becker, A. N. Dinkelaker, J. Grosse, O. Hellmig, H. Müntinga, V. Schkolnik, S. T. Seidel, T. Wendrich *et al.*, Ultracold atom interferometry in space, Nat. Commun. **12**, 1317 (2021).
[32] M. Elsen, B. Piest, F. Adam, O. Anton, P. Arciszewski, W. Bartosch, D. Becker, K. Bleeke, J. Böhm, S. Boles *et al.*, A dual-species atom interferometer payload for operation on sounding rockets, Microgravity Sci. Technol. **35**, 48 (2023).
[33] B. Barrett, L. Antoni-Micollier, L. Chichet, B. Battelier, T. Léveque, A. Landragin, and P. Bouyer, Dual matter-wave inertial sensors in weightlessness, Nat. Commun. **7**, 13786 (2016).
[34] M. Jaffe, V. Xu, P. Haslinger, H. Müller, and P. Hamilton, Efficient adiabatic spin-dependent kicks in an atom interferometer, Phys. Rev. Lett. **121**, 040402 (2018).
[35] S.-W. Chiow, T. Kovachy, H.-C. Chien, and M. A. Kasevich, $102\hbar k$ large area atom interferometers, Phys. Rev. Lett. **107**, 130403 (2011).
[36] M. Gebbe, J.-N. Siemß, M. Gersemann, H. Müntinga, S. Herrmann, C. Lämmerzahl, H. Ahlers, N. Gaaloul, C. Schubert, K. Hammerer *et al.*, Twin-lattice atom interferometry, Nat. Commun. **12**, 2544 (2021).
[37] J. McGuirk, M. Snadden, and M. Kasevich, Large area light-pulse atom interferometry, Phys. Rev. Lett. **85**, 4498 (2000).
[38] J. Lee, R. Ding, J. Christensen, R. R. Rosenthal, A. Ison, D. P. Gillund, D. Bossert, K. H. Fuerschbach, W. Kindel, P. S. Finnegan *et al.*, A compact cold-atom interferometer with a high data-rate grating magneto-optical trap and a photonic-integrated-circuit-compatible laser system, Nat. Commun. **13**, 5131 (2022).
[39] X. Cheng, Building a sensitive atom interferometer for navigation, Ph.D. thesis, Imperial College London, 2020.
[40] D. O. Sabulsky, I. Dutta, E. A. Hinds, B. Elder, C. Burrage, and E. J. Copeland, Experiment to detect dark energy forces using atom interferometry, Phys. Rev. Lett. **123**, 061102 (2019).
[41] G. Peng, A sensitive horizontal atom interferometer for testing acceleration from an in-vacuum source mass, Ph.D. thesis, Imperial College London, 2023.
[42] D. S. Weiss, B. C. Young, and S. Chu, Precision measurement of $\hbar/m_{\rm Cs}$ based on photon recoil using laser-cooled atoms and atomic interferometry, Appl. Phys. B **59**, 217 (1994).
[43] See Supplemental Material at http://link.aps.org/supplemental/10.1103/ghlb-v3jc for the derivation of our trapezoidal acceleration weighing function, which includes Refs. [44,47–49].
[44] J. M. Hogan, D. M. Johnson, and M. A. Kasevich, Light-pulse atom interferometry, in *Atom Optics and Space Physics*, edited by E. Arimondo, W. Ertmer, W. P. Schleich, and E. M. Rasel (IOS, Amsterdam, 2009), pp. 411–447.
[45] When the Raman beams are horizontal, the σ^+–σ^+ and σ^-–σ^- Raman transitions are degenerate in frequency and have opposite recoil momenta. It is therefore necessary to suppress one of them to avoid splitting the wavefunction at each π-pulse. It is not necessary if the beams are vertical because then the Doppler shift removes the frequency degeneracy.
[46] G. Peng, B. Lanigan, R. Shah, J. Lim, A. Kaushik, J. Cotter, E. A. Hinds, and B. E. Sauer, Data for the paper "A large-momentum-transfer Raman atom interferometer without k-reversal" [Dataset], Zenodo (2025), doi: 10.5281/zenodo.15780990.
[47] P. Storey and C. Cohen-Tannoudji, The Feynman path integral approach to atomic interferometry: A tutorial, J. Phys. II **4**, 1999 (1994).
[48] B. Barrett, P.-A. Gominet, E. Cantin, L. Antoni-Micollier, A. Bertoldi, B. Battelier, P. Bouyer, J. Lautier, and A. Landragin, Mobile and remote inertial sensing with atom interferometers, in *Atom Interferometry*, edited by G. M. Tino and M. A. Kasevich (IOS, Amsterdam; SIF, Bologna, 2014), pp. 493–555.
[49] J. Beitia, A. Clifford, C. Fell, and P. Loisel, Quartz pendulous accelerometers for navigation and tactical grade systems, in *2015 DGON Inertial Sensors and Systems Symposium (ISS)* (IEEE, Karlsruhe, Germany, 2015), pp. 1–20.